第 38 卷 第 6 期　　分 子 催 化 (中 英 文)　　Vol.38,No.6
2024 年 12 月　　JOURNAL OF MOLECULAR CATALYSIS(CHINA)　　Dec.　2024

Article ID：1001-3555(2024)06-0510-11　　*Articles*

Synthesis of A-position Ba-doped Perovskite $LaCoO_3$ and Performance of Photocatalytic Phenol Degradation

YUAN Li-jing[1], ZHAO Kun-feng[2], SONG Jin[3], GUO Shi-long[3], GUO Jia-le[3], WANG Yan[3], MENG Xian-jie[4], WEI Xian-xian[5], LIU Zhen-min[3], WANG Xiao-xiao[3*]

(1. School of Energy & Materials Engineering, Taiyuan University of Science and Technology, Taiyuan 030024, China; 2. Wenzhou Aids to Navigation Division, Donghai Navigation Safety Administration (DNSA), Wenzhou 035000, China; 3. School of Chemical Engineering and Technology, Taiyuan University of Science and Technology, Taiyuan 030024, China; 4. College of Chemical Engineering and Technology, Taiyuan University of Technology, Taiyuan 030024, China; 5. School of Environment and Resources, Taiyuan University of Science and Technology, Taiyuan 030024, China)

Abstract: The utilization of perovskite oxide materials as catalysts for the photodegradation of organic pollutants in water is a promising and rapidly advancing field. In this study, a series of $La_{1-x}Ba_xCoO_3$ (x=0.2, 0.3, 0.4, 0.5, 0.6) catalysts with varying Ba doping ratios were synthesized using the citric acid complexation-hydrothermal synthesis combined method for the degradation of phenol under visible light irradiation. Among the synthesized catalysts, $La_{0.5}Ba_{0.5}CoO_3$ exhibited the highest photocatalytic activity. In addition, the photocatalytic mechanism for $La_{0.5}Ba_{0.5}CoO_3$ perovskite degradation of phenol was also discussed. The synthesized catalysts were characterized using XRD, SEM, FT-IR, XPS, MPMS and other characterization techniques. The results revealed that the diffraction peak intensity of $La_{1-x}Ba_xCoO_3$ increased with higher Ba doping ratios, and the $La_{0.4}Ba_{0.6}CoO_3$ exhibited the strongest diffraction peaks. The catalyst particle sizes ranged from 10 to 50 nm, and the specific surface area decreased with increasing Ba content. Additionally, the paramagnetic properties of $La_{0.5}Ba_{0.5}CoO_3$ were similar to that of $La_{0.4}Ba_{0.6}CoO_3$. The experimental results suggested that the incorporation of Ba could significantly improve the catalytic performance of $La_{1-x}Ba_xCoO_3$ perovskites, promote electron transfer and favor to the generation of hydroxyl radicals (•OH), leading to the efficiently degradation of phenol.

Key words: perovskite catalyst; $La_{1-x}Ba_xCoO_3$; photocatalysis; phenol degradation; mechanism

CLC number: O643.32　　**Document code:** A　　**DOI:** 10.16084/j.issn1001-3555.2024.06.002

Phenol, as a vital industrial chemical product, is well known for its bio-treatment of recalcitrant and acute toxicity. The ubiquitous presence of phenol in wastewater and its associated environmental risks have raised significant public health concerns[1]. Phenol is continuously discharged into aquatic environments through various anthropogenic activities. Its presence in storm and wastewater effluent poses a major obstacle to the widespread adoption of water recycling[2−3]. Moreover, it can directly harm ecosystems and endanger human health through the contamination of drinking water sources, including surface and groundwater[4]. Consequently, developing effective strategies for the removal of persistent phenol from wastewater effluent is crucial to minimize pollution risks.

Currently, numerous efforts have been devoted to developing suitable methods for removing phenol from wastewater effluent[5−12]. In recent years, photocatalytic degradation of phenol has emerged as a prominent research area. As an advanced oxidation technology, photocatalytic degradation has garnered significant attention due to its ability to efficiently degrade organic compounds in wastewater without generating secondary pollution[7−11]. However, conventional photocatalysts like TiO_2 and ZnO are unable to fully utilize visible light, which constitutes approximately 45% of the solar spectrum, and thus fail to meet the rapidly increasing energy demand. This limitation has spurred extensive research into the development and exploration of efficient visible-light-driven photocatalysts to utilize solar energy more effectively.

Perovskite oxide semiconductors (ABO_3) have shown great potential as photocatalysts, due to their excellent absorption of solar energy, particularly in the visible light spectrum, and their high quantum efficiency[13−16]. The term “perovskite” refers to the crystal structure of calcium titanate ($CaTiO_3$), discovered by Gustav Rose in 1839 and named in honor of Lev Perovski[17]. In perovskite structures, the A-site typically accommodates rare earth or alkali metals with larger ionic radii, while the B-site is occupied by transition metals with smaller ionic radii.

According to the literature, doping, as a modification

Received date: 2024-09-29; **Revised date:** 2024-11-07.

Foundation: The Fundamental Research Program for Young Scientists of Shanxi Province (Project No. 202103021223294); The Fundamental Research Program of Shanxi Province (Project No. 202203021211203); The Start-up Fund for Doctorate Scientific Research Project of Taiyuan University of Science and Technology (Project No. 20232124); The Innovation and Entrepreneurship Training Program for Undergraduate, Taiyuan University of Science and Technology (Project No. DCX2024162).

Biography: Yuan Li-jing (1992−), male, PhD, mainly engaged in the clean use of traditional energy sources. E-mail: 2023056@tyust.edu.cn.

* Corresponding authors. E-mail: xxwang@tyust.edu.cn.

method, has been shown to enhance the catalytic properties of perovskites. By introducing metal dopants at either the A or B sites, the lattice structure can be modified, indirectly influencing and improving the activity and mobility of lattice oxygen, which in turn enhances catalytic performance[18−24]. For example, Wang *et al.*[18] synthesized $BiCo_xFe_{1-x}O_3$ by doping Fe into $BiCoO_3$, demonstrating a significant increase in magnetization due to Co substitution for Fe ions, while DTA confirmed the preservation of ferroelectric properties. Fan *et al.*[19] prepared $La_{1-x}Ce_xMnO_3$ perovskites with varying Ce doping ratios for catalytic ozonation of phenol and found that $La_{0.9}Ce_{0.1}MnO_3$ exhibited superior catalytic performance and good reusability. Huang *et al.*[20] reported the synthesis of $LaCu_xFe_{1-x}O_3$ with different Fe doping ratios for the removal of organic pollutants, achieving optimal performance with 0.4 Fe doping at a gelation temperature of 80 ℃ and calcination temperature of 700 ℃, resulting in a 91.64% COD removal rate in cellulosic ethanol wastewater. Bouchal *et al.*[21] prepared via a sol-gel method with different concentrations of Bi nitrate and examined as a photocatalyst for RhB degradation under sunlight, and its antioxidant and antibacterial activities were examined. The results showed that the highest degradation rate was exhibited by 15% Bi-doped $BaBiO_3$ for the degradation of RhB under solar radiation. According to the antibacterial activity study, the addition of Bi enhanced the antibacterial activity of the resulting material against both Gram-positive and Gram-negative microorganisms.

Based on the previous experimental findings, the results indicated $LaCoO_3$ perovskite catalyst exhibited a certain photocatalytic activity for phenol, and the degradation rate reached 52.56% with 4 h irradiation. To further improve the performance of $LaCoO_3$ catalysts, this study focused on doping Ba into the A-site of $LaCoO_3$ to synthesize $La_{1-x}Ba_xCoO_3$ catalysts. The physical and chemical properties of these A-site doped materials were characterized and analyzed to understand the effect of doping on their catalytic behavior. Furthermore, the photocatalytic degradation of phenol under visible light irradiation was investigated to evaluate the efficacy of the doped perovskites.

1 Experimental section

1.1 Materials

Lanthanum nitrate ($La(NO_3)_3\cdot 6H_2O$, AR, 99%), cobalt nitrate ($Co(NO_3)_2\cdot 6H_2O$, AR, 99%), barium nitrate ($Ba(NO_3)_2$, AR, 99%), phenol (AR), citric acid (AR, ⩾99.5%), ammonia (AR, 25%), ethanol (AR, ⩾99.7%). The phenol solution was prepared into distilled water.

1.2 Catalyst preparation

The specific preparation method of modified $LaCoO_3$ catalyst is citric acid complexation-hydrothermal synthesis combined method and as follows: (ⅰ) Solution preparation: 80 mL of deionized water was added to a beaker. $La(NO_3)_3\cdot 6H_2O$, $Ba(NO_3)_2$, $Co(NO_3)_2\cdot 6H_2O$, and citric acid were accurately weighed and dissolved in the water, maintaining the stoichiometric ratio of $La_{1-x}Ba_xCoO_3$ (x = 0.2, 0.3, 0.4, 0.5, 0.6). The molar ratio of $n(La^{3+}+Ba^{2+}) : n(Co^{2+}) : n$(citric acid) was kept at 1 : 1 : 1; (ⅱ) pH adjustment and complexation: The solution was stirred continuously at a uniform speed on a magnetic stirrer for 1 h to ensure complete complexation of the metal ions with citric acid. Meanwhile ammonia solution was added dropwise to the stirred solution to adjust the pH to approximately 8.5. This alkaline environment facilitated the complete precipitation of the metal ions as hydroxides; (ⅲ) Hydrothermal reaction: The mixture was poured into a teflon stainless steel container and reacted in an oven at 150 ℃ for 20 h; (ⅳ) Washing and drying: After the hydrothermal reaction, the resulting precipitate was removed from the teflon stainless steel container, centrifuged to separate it from the liquid, and washed thoroughly with deionized water to remove any residual reactants. The precipitate was then dried in an oven at 120 ℃; (ⅴ) Calcination: The dried precipitate was ground into a fine powder and calcined at 750 ℃ for 2 h. This high-temperature treatment removed any remaining organic matter and facilitated the formation of the final perovskite crystal structure; (ⅵ) Labeling: The synthesized catalysts were labeled as Ba-0.2, Ba-0.3, Ba-0.4, Ba-0.5 and Ba-0.6, corresponding to their respective Ba doping ratios (x values in $La_{1-x}Ba_xCoO_3$). The specific synthesis flowchart was shown in Fig.1.

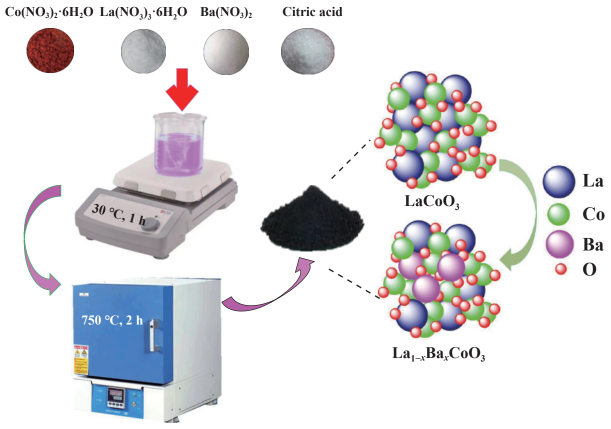

Fig.1 $La_{1-x}Ba_xCoO_3$ synthesization flowchart

1.3 Catalyst characterization

X-ray powder diffraction (XRD): Crystalline phases and crystal structure of the synthesized catalysts were determined using a Rigaku D/max-2500 X-ray diffractometer. The diffractometer was operated with Cu Kα radiation (λ = 0.154 18 nm) generated at 40 kV and 100 mA. Diffraction patterns were collected in the 2θ range of 5° to 90° with a scanning rate of 0.02 $(°)\cdot s^{-1}$; Scanning electron microscopy (SEM) and energy-dispersive X-ray spectroscopy (EDS): Surface morphology, particle size, and elemental composition of the catalysts were analyzed using a LEO-435VP scanning electron microscope equipped with an energy-dispersive X-ray spectrometer (EDS). The microscope was operated at an accelerating voltage of 20 kV; Fourier transform infrared spectroscopy (FT-IR): The functional groups present in the catalysts were identified using a Nicolet 380 FTIR spectrometer. Spectra were acquired in transmission mode over the wavenumber 4 000 to 400 cm^{-1} with a resolution of 4.0 cm^{-1}; N_2 adsorption-desorption isotherms: Specific surface area was determined by applying the Brunauer-Emmett-Teller (BET) model to the N_2 adsorption isotherms measured at −196 ℃ using a Micromeritics Tristar 3000 instrument. Pore size distributions were calculated using the Barrett-Joyner-Halenda (BJH) model applied to the desorption branch of the isotherms. Prior to analysis, samples were outgassed under vacuum at 300 ℃ for 3 h; X -ray photoelectron spectroscopy (XPS): Surface chemical composition and oxidation states of elements in the catalysts were investigated using a Kratos Axis Ultra DLD spectrometer equipped with a monochromatic Al Kα X-ray source (1 486.6 eV). High-resolution spectra were acquired with pass energy of 20 eV. The binding energy scale was calibrated using the C 1*s* peak at 284.8 eV. Peak fitting and deconvolution were performed using CasaXPS software with a Shirley background subtraction; Magnetic property measurement system (MPMS): Magnetic properties of the powdered catalysts were measured using a Quantum Design MPMS-XL SQUID magnetometer. The magnetization was measured as a function of temperature (−271.15~26.85 ℃) and applied magnetic field (−5 to 5 T).

1.4 Photocatalytic activity tests

The photocatalytic activity of the synthesized $La_{1-x}Ba_xCoO_3$ catalysts was evaluated by monitoring the degradation of phenol in aqueous solution (100 mL, 10 mg·L^{-1}) under visible light irradiation. All experiments were conducted at a constant temperature of 20 ℃ using a jacketed beaker with continuous water circulation to maintain the temperature. The solution was continuously stirred magnetically and ventilated throughout the experiment. A PLS-SXE300 xenon lamp equipped with a cutoff filter was used as the visible light source.

Experimental procedure: (Ⅰ) Dark adsorption: 100 mg of the synthesized photocatalyst was dispersed in 100 mL of the phenol solution in the jacketed beaker. The dispersion was stirred in the dark for 40 min to ensure adsorption-desorption equilibrium between phenol and the catalyst surface; (Ⅱ) Photocatalytic reaction: The dispersion was then irradiated with visible light. At predetermined time intervals of 30 min, 2 mL of the specified dispersion was withdrawn from the reaction mixture and filtered through a 0.22 μm syringe filter to remove the catalyst particles; (Ⅲ) UV-Vis spectrophotometry: The concentration of phenol in the filtered aliquots was determined by measuring the absorbance at 270 nm using a UV-2550 spectrophotometer. A calibration curve was constructed using standard phenol solutions to relate absorbance to concentration; (Ⅳ) Control experiments: Control experiments were performed under identical conditions but in the absence of visible light irradiation and without the addition of the photocatalyst; (Ⅴ) Degradation efficiency calculation: The photocatalytic degradation efficiency (*D*) was calculated using the following equation (1):

$$D = \frac{(C_0 - C_t)}{C_0} \times 100\% \quad (1)$$

where C_0 is the initial concentration of phenol, and C_t is the concentration at time *t*.

2 Results and discussion

2.1 Structure characterization

The phase structure of prepared samples were analyzed by XRD, and the XRD pattern of catalysts with different Ba doping ratios were compared with the standard spectra (in Fig.2). It can be found that the characteristic diffraction peaks of $LaCoO_3$ in the 2θ of 23.79°, 26.18°, 32.90°, 40.54°, 47.41°, 58.77°, 69.07° and 78.78° were attributed to (110), (111), (200), (211), (220), (222), (400) and (420) lattice planes (JPCDS No.32-0480)[25], respectively. XRD results showed that $LaCoO_3$ was successfully synthesized by citric acid complexation-hydrothermal synthesis combined method. Notably, no additional peaks corresponding to impurities or secondary phases were observed, confirming the phase purity of the synthesized catalysts. Furthermore, Fig.2 demonstrated a gradual increase in the intensity of diffraction peaks with increasing Ba doping ratio, and the Ba-0.6 showed the strongest diffraction peaks. This observation suggested that Ba successfully substituted La in the perovskite lattice. Due to the larger ionic radius of Ba compared to La, the lattice parameters expanded, leading to a slight shift of the XRD pattern towards lower angles.

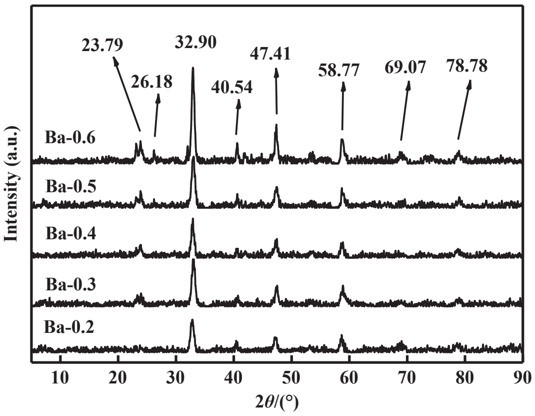

Fig.2 XRD patterns of the synthesized A-site Ba doped $LaCoO_3$ catalysts

The morphology and microstructure of modified $LaCoO_3$ samples were studied by SEM. The distribution of elements within the samples was further analyzed using EDS spectroscopy. SEM images of the Ba-0.2, Ba-0.3, Ba-0.4, Ba-0.5, Ba-0.6 and $LaCoO_3$ catalysts were presented in Fig.3(a–f),

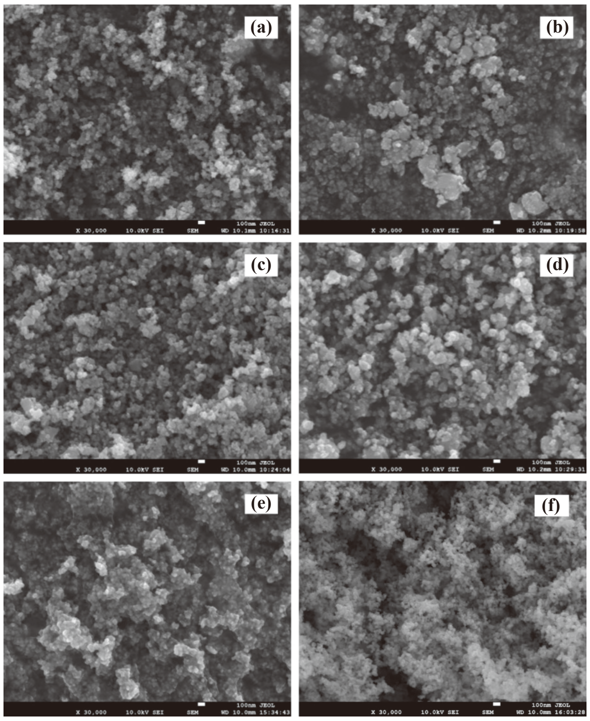

Fig.3 SEM of modified $LaCoO_3$ catalysts (a) Ba-0.2, (b) Ba-0.3, (c) Ba-0.4, (d) Ba-0.5, (e) Ba-0.6, (f) $LaCoO_3$

respectively. These images revealed a general trend of increasing average particle size with increasing Ba doping ratio. Notably, the Ba-0.6 catalyst exhibited the largest particle size, ranging from 20 to 50 nm, with a certain degree of agglomeration observed between the particles, which further illustrated that the Ba doping could increase the catalyst particle size. The smaller size was beneficial to the transfer of photo-generated electrons and enhancement of the photocatalytic performance[26]. The EDS was employed to analyze the elemental composition of the modified $LaCoO_3$ catalysts. The EDS spectrum of the Ba-0.5 catalyst in Fig.4, revealed the presence of La, Ba, Co, O and C. The atomic percentages of these elements were determined to confirm the successful incorporation of Ba into the perovskite lattice. Table 1 presented the elemental ratios, which closely approximate the expected stoichiometry of (La+Ba) ∶ Co ∶ O = 1 ∶ 1 ∶ 3 for the perovskite ABO_3 structure. This finding confirms the successful doping of Ba into the $LaCoO_3$ lattice. Notably, the Ba-0.5 catalyst exhibited an elemental ratio closest to the ideal 1 ∶ 1 ∶ 3 stoichiometry among the five synthesized catalysts, suggesting a higher degree of purity. This enhanced purity may contribute to the superior photocatalytic performance observed for the Ba-0.5 catalyst.

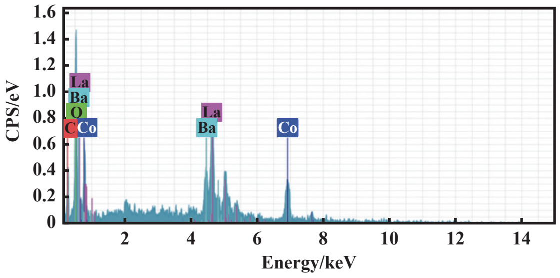

Fig.4 EDS of Ba-0.5 catalyst

Table 1 Atomic content (mole fraction) of $LaCoO_3$ and modified $LaCoO_3$ catalysts

Catalyst	Atomic content (mole fraction)/ %		
	La+Ba	Co	O
$LaCoO_3$	14.4	14.0	58.2
Ba-0.2	14.1	11.2	63.0
Ba-0.3	12.1	9.5	59.3
Ba-0.4	17.1	14.4	48.9
Ba-0.5	18.2	16.8	48.2
Ba-0.6	11.8	15.2	54.5

The FT-IR spectroscopy was employed to identify the functional groups in the catalysts. The FT-IR spectra of the catalysts with different Ba doping ratios were shown in Fig.5, and the corresponding peak assignments were listed in Table 2. The peak at approximately 417 cm^{-1} corresponded to the bending vibration of O—Co—O in the perovskite ABO_3 structure, while the peak at about 550 cm^{-1} was attributed to the stretching vibration of Co—O[27]. The strong absorption peak at 602 cm^{-1} further confirmed the presence of Co—O stretching vibrations in the ABO_3 phase[28]. A weak absorption peak observed at about 850 cm^{-1} suggests the presence of carbonate species[29], likely originating from residual carbon and oxygen impurities introduced during the synthesis process using citric acid as the complexing agent. Notably, the Co—O stretching vibration peak at 550 cm^{-1} gradually shifted to lower wavenumbers with increasing Ba doping ratio, indicating a weakening of the Co—O bond covalency and an increase in ionic character upon Ba incorporation[30]. This observation can be attributed to lattice strain induced by lattice distortion due to the larger ionic radius of Ba compared to La. The FT-IR results, in conjunction with XRD and other characterization data, provided further evidence for the successful doping of Ba into the $LaCoO_3$ crystal structure.

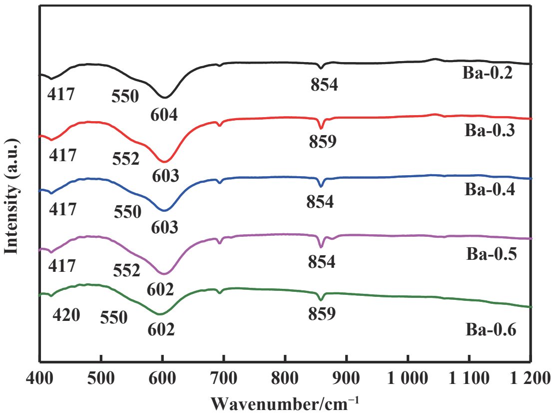

Fig.5 Infrared spectrogram attribution analysis of modified $LaCoO_3$ catalysts

Table 2 Infrared spectrum attribution analysis of modified $LaCoO_3$ catalysts

Catalyst	Wavenumber/cm^{-1}		
	O—Co—O	Co—O	
Ba-0.2	417	550	604
Ba-0.3	417	552	603
Ba-0.4	417	550	603
Ba-0.5	417	552	602
Ba-0.6	420	550	602

The textural properties of the modified $LaCoO_3$ catalysts, as determined by N_2 adsorption-desorption isotherms, were summarized in Table 3. The specific surface areas of the synthesized samples were relatively low, likely due to the presence of citric acid during synthesis. As shown in Table 3, the specific surface area of the catalysts decreased with increasing Ba doping ratio. Among the prepared catalysts, Ba-0.2 exhibited the highest specific surface area (23.95 $m^2 \cdot g^{-1}$), along with the largest pore volume and pore size. This decrease in textural properties with increasing Ba content may be attributed to the increased energy required for interdiffusion between grains in the presence of $Ba(NO_3)_2$[31, 32]. The presence of Ba ions could hinder the direct contact between crystal particles and impede crystal growth, leading to a reduction in both specific surface area and pore size[33]. There were research findings indicating that specific surface area of photocatalyst was related with its photocatalytic performance. A larger specific surface area was beneficial for the contact between the

Table 3 Pore structure parameters of modified $LaCoO_3$ catalysts

Catalyst	$S_{BET}/(m^2\cdot g^{-1})$	$V_{Pore}/(cm^3\cdot g^{-1})$	D_{Pore}/nm
Ba-0.2	23.95	0.126	20.98
Ba-0.3	18.57	0.080	19.35
Ba-0.4	17.94	0.080	16.98
Ba-0.5	16.43	0.064	14.71
Ba-0.6	6.84	0.025	14.31

catalyst and the reaction solution, thereby improving the photocatalytic performance of the catalyst.

The N_2 adsorption-desorption isotherms and pore size distributions of the $LaCoO_3$ catalysts with different Ba doping ratios were presented in Fig.6. According to the IUPAC classification, all catalysts exhibited Ⅳ type isotherms, characteristic of mesoporous materials. The presence of H3 hysteresis loops in the catalysts, with closure points in the p/p_0 between 0.1 and 0.2, indicated the presence of slit-shaped pores or plate-like particles. Furthermore, the pore size distributions revealed that all the catalysts possessed mesopores with sizes ranging from 2 to 50 nm. The gradual decrease in adsorption volume with increasing Ba doping ratio suggested a corresponding decrease in the specific surface area of the catalysts. This observation was consistent with the SEM analysis, which showed an increase in particle size and agglomeration with higher Ba content, leading to a reduction in the available surface area.

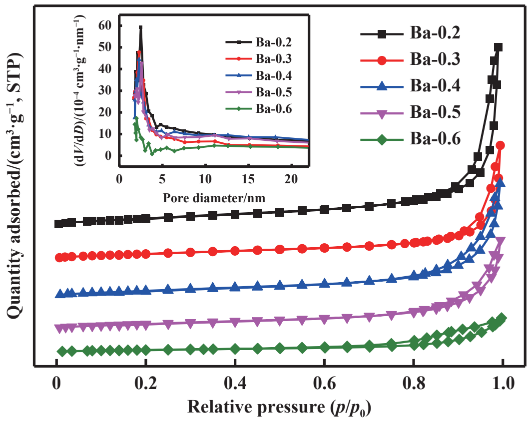

Fig.6 Adsorption desorption curve and BJH pore size distribution of $La_{1-x}Ba_xCoO_3$ catalysts ($x = 0.2, 0.3, 0.4, 0.5, 0.6$)

XPS was employed to investigate the elemental composition and valence states of the $La_{1-x}Ba_xCoO_3$ (x=0.2, 0.3, 0.4, 0.5, 0.6) catalysts. The XPS survey spectra (Fig.7(a)) confirmed the presence of La, Co, Ba, O and C, consistent with the EDS analysis. The carbon signal (C 1*s*) was used as a reference for binding energy calibration.

The La 3*d* spectra in Fig.7(b) exhibited two characteristic peaks, La $3d_{5/2}$ and La $3d_{3/2}$ separated by approximately 4 eV due to spin-orbit coupling. Each of these peaks was further resolved into two components, arising from the transfer of electrons from the oxygen valence band to the empty La 4*f* orbital during the ionization process[34]. The La 3*d* XPS spectra confirmed the presence of La in the trivalent oxidation state[35], indicating that it did not participate in redox reactions as an active site. The Ba 3*d* spectra (Fig.7(c)) displayed two peaks, the binding energy centered at 795.1 and 779.65 eV ascribed to Ba $3d_{3/2}$ and Ba $3d_{5/2}$ respectively, with a separation of 15.4 eV, consistent with literature values[36]. Each peak was further resolved into two components, separated by approximately 3 eV, corresponding to Ba in the bivalent oxidation state[37−40]. The Co 2*p* spectra (Fig.7(d)) exhibited four peaks at 778.9, 781.6, 793.9, and 796.8 eV, attributed to Co^{3+} and Co^{2+} species, respectively. The peak at 790.0 eV was assigned to the satellite peak of Co^{2+}, while the peak at 805.1 eV was ascribed to the satellite peak of Co species in Co_3O_4[41−42].

Finally, the O 1*s* spectra (Fig.7(e)) was deconvoluted into three peaks located at 528.9, 531.3 and 532.8 eV, corresponding to lattice oxygen, oxygen vacancies, and surface-adsorbed oxygen, respectively[43]. The presence of oxygen vacancies was noteworthy as it could significantly influence the catalytic activity of the perovskite materials.

The magnetic properties of the $La_{1-x}Ba_xCoO_3$ catalysts were investigated by measuring their magnetic hysteresis loops at room temperature (Fig.8). As La and Co were known to exhibit magnetic behavior, the observed strong linear M-H curves passing through the origin are indicative of paramagnetic behavior in these catalysts[44−46]. The modified $LaCoO_3$ catalyst displayed a relatively strong paramagnetism, with an increasing trend observed as the Ba doping ratio increased. Notably, the Ba-0.5 and Ba-0.6 catalysts exhibited the highest paramagnetic susceptibility among the samples, suggesting a potential correlation between Ba content and the density of unpaired electrons responsible for paramagnetism. While the observed paramagnetism may be associated with enhanced catalytic activity, it was not the sole determining factor, as other factors such as surface area and crystal structure also play crucial roles. Nevertheless, the strong paramagnetic nature of the catalysts presents an opportunity for their efficient recovery and recycling using magnetic separation techniques, thereby reducing costs and promoting the sustainability of the photocatalytic process.

2.2 Photocatalytic performance

The photocatalytic activity of $LaCoO_3$ and $La_{1-x}Ba_xCoO_3$ catalysts with different Ba doping ratios were assessed by degradation of phenol under visible light irradiation. As shown in Fig.9(a), the degradation rate of phenol initially increased and then decreased as the Ba doping ratio increased, indicating an optimal Ba content beneficial for photocatalytic performance. The Ba-0.5 catalyst exhibited the highest photocatalytic activity, achieving the phenol degradation rate of 83.50% after 6 h irradiation at 20 ℃. In contrast, the Ba-0.2 catalyst showed the lowest degradation rate (28.09%), while the Ba-0.3, Ba-0.4 and Ba-0.6 catalysts achieved degradation rates of 36.92%, 54.07% and 63.40%, respectively, under the same conditions. To elucidate the role of the Ba-0.5 photocatalyst in phenol degradation and to differentiate the contributions of adsorption and photocatalysis, a comparative experiment was conducted with and without visible light irradiation. As depicted in Fig.9(b), in the absence of light, the Ba-0.5 catalyst adsorbed approximately 10% of phenol, and this adsorption capacity had no change over 6 h. Moreover, the degradation rate of phenol significantly increased to over 80% under visible light irradiation. The results demonstrated that the Ba-0.5 catalyst exhibited high photocatalytic activity towards phenol, and the adsorption played a minor role in the overall degradation process.

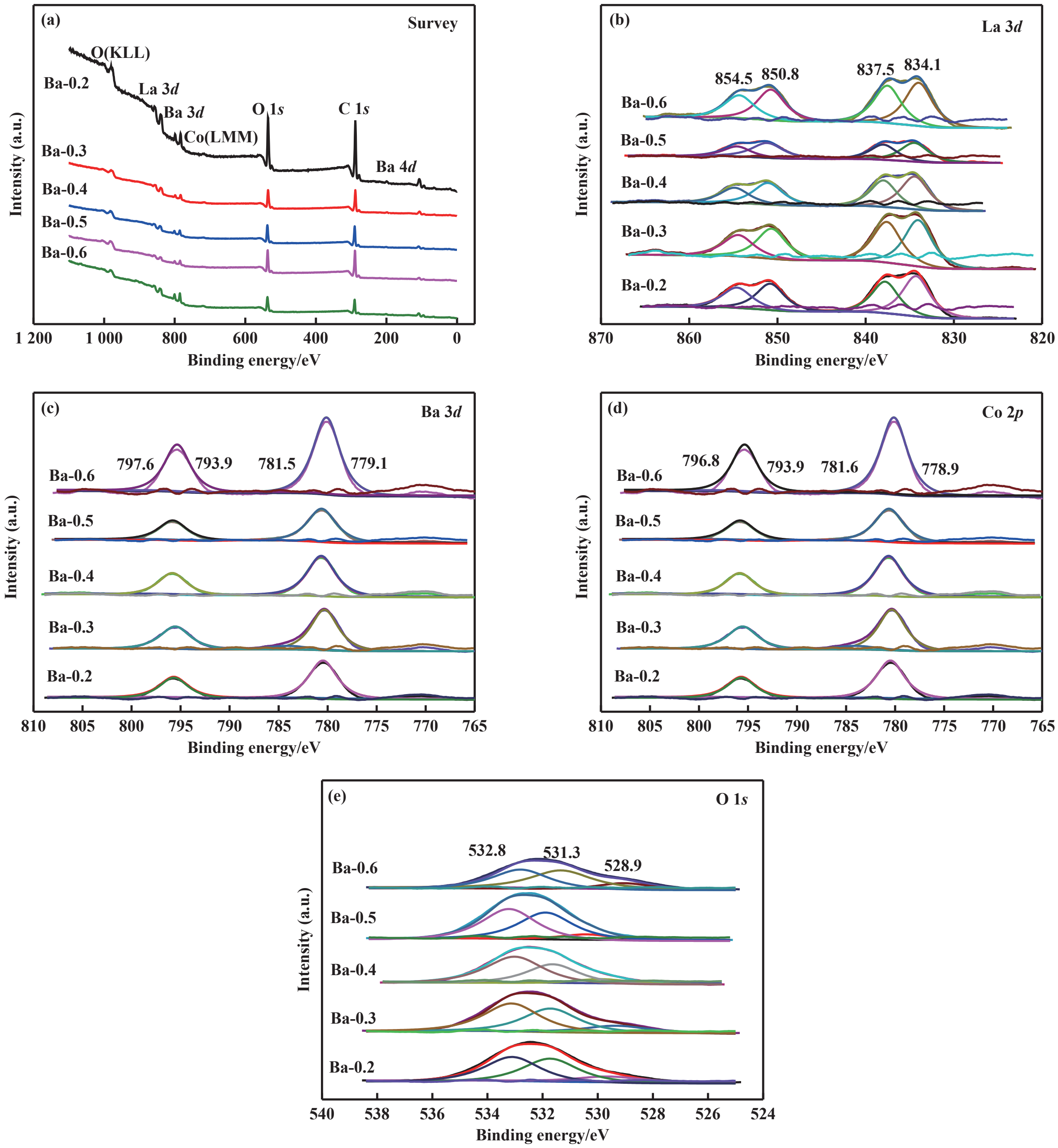

Fig.7 XPS analysis energy spectrum of modified $LaCoO_3$ catalysts (a) survey, (b) La 3*d*, (c) Ba 3*d*, (d) Co 2*p*, (e) O 1*s*

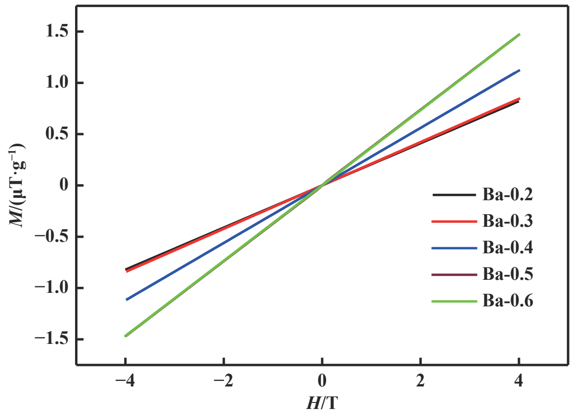

Fig.8 MPMS diagram of modified $LaCoO_3$ catalysts

2.3 The degradation kinetics curve of phenol

To further corroborate the observed photocatalytic activities, the degradation kinetics of phenol by the $La_{1-x}Ba_xCoO_3$ catalysts were investigated. The linear relationship between $\ln(C_0/C)$ and irradiation time (t) was given in Fig.10(a), indicated that the photodegradation of phenol follows pseudo-first-order kinetics. This kinetic model suggested that the rate of phenol degradation was directly proportional to its concentration, with the photocatalyst acting as a constant factor. The rate constant (k) for each catalyst could be determined from the slope of the linear fit in Fig.10(a)[47].

$$r = kC_A \tag{2}$$

$$r = -\frac{d(C_A)}{dt} \tag{3}$$

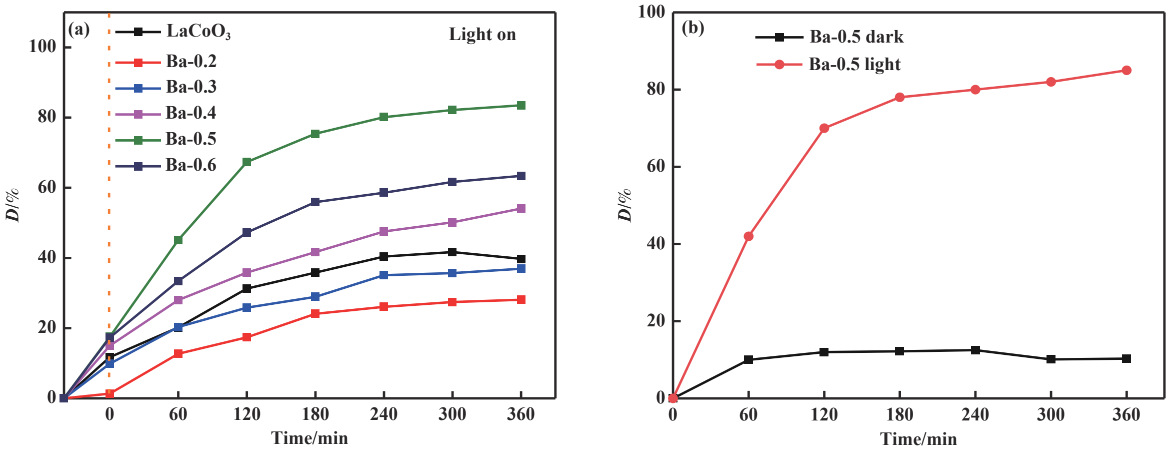

Fig.9 (a) Degradation rate curves of different Ba doped LaCoO$_3$ catalysts for photocatalytic degradation of phenol; (b) Degradation of phenol under different conditions of Ba-0.5

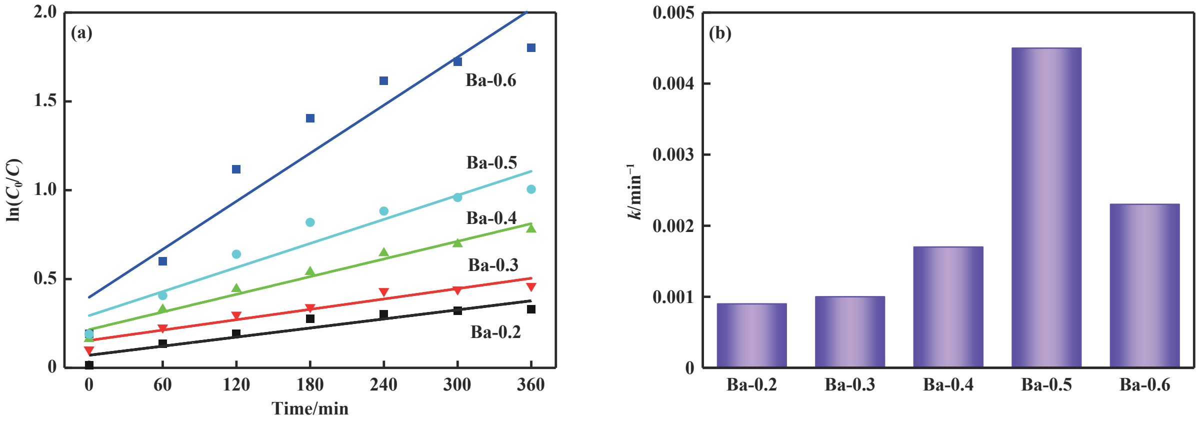

Fig.10 The corresponding kinetic plots of phenol degradation over different catalysts (a) linear relationship between ln(C_0/C) and t, (b) rate constants corresponding to different catalysts

$$-\frac{d(C_A)}{dt} = kC_A \qquad (4)$$

$$-\int_{C_{A0}}^{C_A} \frac{1}{C_A} = \int_{t_0}^{t} k\cdot dt \qquad (5)$$

$$\therefore \ln(C_0/C) = kt \qquad (6)$$

The rate constants (k) for phenol degradation by the different $La_{1-x}Ba_xCoO_3$ catalysts, derived from the slopes of the linear fits in Fig.10(a), were presented in Fig. 10(b). The Ba-0.5 catalyst exhibited the highest rate constant (0.004 5 min^{-1}), demonstrating superior photocatalytic activity compared to the other catalysts. The rate constants for Ba-0.2, Ba-0.3, Ba-0.4 and Ba-0.6 were 0.000 9, 0.001 0, 0.001 7 and 0.002 3 min^{-1}, respectively. Notably, the Ba-0.5 catalyst exhibited a rate constant approximately 5, 4.5, 2.7 and 2.0 times higher than that of Ba-0.2, Ba-0.3, Ba-0.4 and Ba-0.6, respectively. This significant enhancement in photocatalytic activity at a La : Ba ratio of 1 : 1 (Ba-0.5) was consistent with the observed trend in phenol degradation efficiency, further confirming the optimal doping ratio for maximizing the catalytic performance of $LaCoO_3$.

2.4 Catalyst reusability

The reusability of the catalyst was a critical factor in assessing its overall effectiveness. To this end, the stability of the Ba-0.5 catalyst was evaluated by recyclability test. The photocatalyst was recycled by filtration, washing and drying for further evaluation. The recovered catalyst (100 mg) was introduced into a 100 mL phenol solution (10 mg·L^{-1}), and its degradation rate was measured using absorbance spectroscopy. As depicted in Fig.11(a), although the degradation rate of phenol displayed a slightly decrease over five cycles, it consistently remained above 70%. This result demonstrates the Ba-0.5 catalyst maintains substantial photocatalytic activity after repeated use. XRD characterization and comparative analysis were then performed on Ba-0.5 before and after five repeated experiments, as shown in Fig.11(b). There was no obvious change could be found in the XRD patterns compared to the used and fresh Ba-0.5 catalyst, suggesting that the crystal structure of Ba-0.5 was well-preserved after five cycles.

2.5 Photocatalytic mechanism

To elucidate the photocatalytic mechanism of the modified Ba-0.5 catalyst in phenol degradation[6, 8, 48−49], the roles of various active radicals in the phenol decomposition process were investigated. Four trapping agents isopropanol (IPA), *p*-benzoquinone (BQ), ammonium oxalate (AO), and silver nitrate ($AgNO_3$) were introduced into the phenol solution under consistent experimental conditions, the agents served as scavengers for hydroxyl radicals (•OH), superoxide radicals ($•O_2^-$), holes (h^+), and photogenerated electrons (e^-), respectively. The results of these trapping experiments were illustrated in Fig.12.

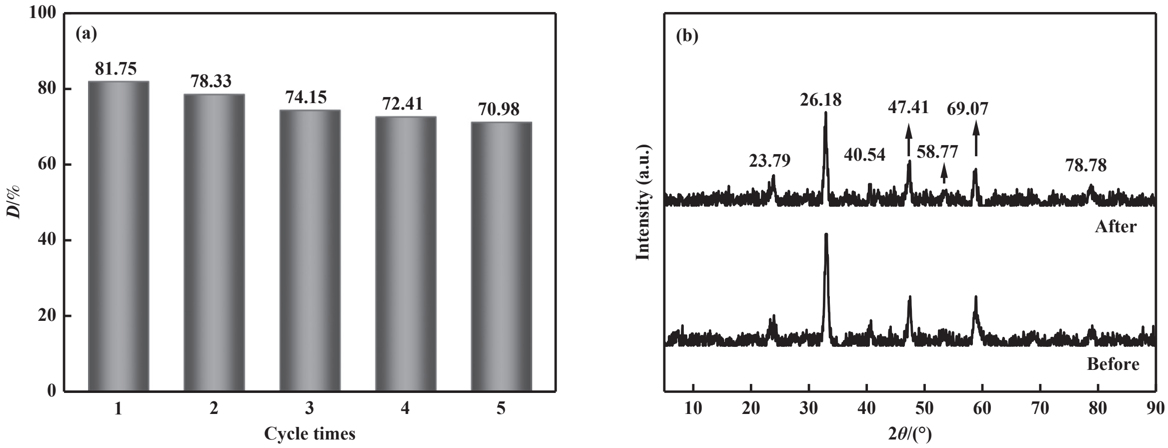

Fig.11 (a) Reusability of the spent Ba-0.5 catalyst and (b) XRD diagram of Ba-0.5 before and after 5 cycles

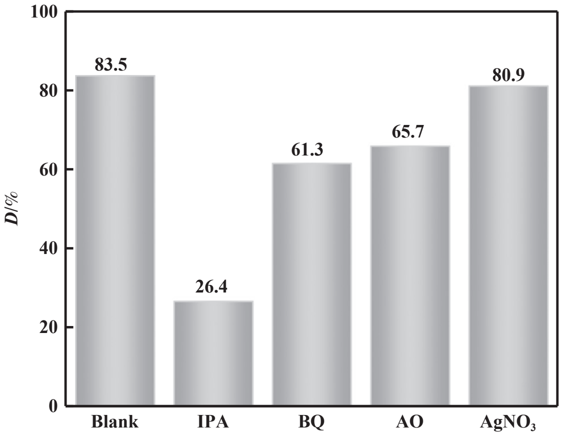

Fig.12 Effect of scavengers on the degradation of phenol

The perovskite-type $LaCoO_3$ photocatalyst was known to exhibit catalytic activity under visible light. Upon irradiation with a xenon lamp, the surface of the $LaCoO_3$ catalyst absorbs photons with energy exceeding its bandgap. This absorption led to the formation of electrons (e^-) in the conduction band and holes (h^+) in the valence band. These charge carriers subsequently reacted with water and oxygen molecules in the system, generating highly reactive species such as hydroxyl radicals (•OH) and superoxide radicals ($\bullet O_2^-$)[50−59]. These radicals could then interact with phenol molecules adsorbed on the catalyst surface, breaking down the organic structure and transforming the phenol into non-polluting small molecules, effectively achieving phenol degradation. The mechanism was as follows:

$$LaCoO_3 + h\nu \rightarrow e^-(LaCoO_3) + h^+(LaCoO_3)$$

$$h^+ + H_2O \rightarrow \bullet OH + H^+$$

$$h^+ + OH^- \rightarrow \bullet OH$$

$$e^- + O_2 \rightarrow \bullet O_2^-$$

$$H_2O + \bullet O_2^- \rightarrow HO_2\bullet + OH^-$$

The results demonstrated that after 6 h of reaction, the phenol degradation rate was 83.5% in the system without a trapping agent. In contrast, the degradation rates were 26.4%, 61.3%, 65.7% and 80.9% in the systems containing IPA, BQ, AO and $AgNO_3$, respectively. This indicated that photo-generated electrons (e^-) had a negligible effect on phenol degradation, while hydroxyl radicals (•OH), superoxide radicals ($\bullet O_2^-$), and holes (h^+) played varying roles in the process. Notably, •OH radicals were the primary contributors to phenol degradation, with $\bullet O_2^-$ and h^+ having relatively minor influences. These reactive species interacted with phenol molecules adsorbed on the catalyst surface, leading to the decomposition of phenol into smaller molecules through three distinct degradation pathways, ultimately achieving photocatalytic degradation of the organic pollutant. The proposed photocatalytic degradation mechanism of phenol was depicted in Fig.13(a), and the $La_{1-x}Ba_xCoO_3$ mechanism diagram was shown in Fig.13(b).

2.6 Synthesis mechanism of $La_{1-x}Ba_xCoO_3$

The $La_{1-x}Ba_xCoO_3$ catalyst was prepared by the citric acid complexation-hydrothermal combined method, and the synthesis mechanism was elucidated through a series of assumptions and rigorous deductions.

Complexation of citric acid with metal ions:

$$C_6H_8O_7 + La^{3+} \rightarrow LaC_6H_5O_7 + 3H^+$$

$$C_6H_8O_7 + Co^{2+} \rightarrow CoC_6H_6O_7 + 2H^+$$

$$C_6H_8O_7 + Ba^{2+} \rightarrow BaC_6H_6O_7 + 2H^+$$

Hydrolysis reaction:

$$LaC_6H_5O_7 \rightarrow LaC_6H_3O_6 + H_2O$$

$$2LaC_6H_3O_6 \rightarrow La_2C_{12}H_6O_{12}$$

$$CoC_6H_6O_7 \rightarrow CoC_6H_4O_6 + H_2O$$

$$2CoC_6H_4O_6 \rightarrow Co_2C_{12}H_8O_{12}$$

$$BaC_6H_6O_7 \rightarrow BaC_6H_4O_6 + H_2O$$

$$2BaC_6H_4O_6 \rightarrow Ba_2C_{12}H_8$$

Oxidation-reduction creaction:

$$La_2C_{12}H_6O_{12} + 9O_2 \rightarrow La_2O_2CO_3 + CO_2 + H_2O$$

$$La_2O_2CO_3 \rightarrow La_2O_3 + CO_2$$

$$3Co_2C_{12}H_8O_{12} + 28O_2 \rightarrow 2Co_3O_4 + 36CO_2 + 12H_2O$$

$$Ba_2C_{12}H_8O_{12} + 9O_2 \rightarrow 2BaO + 12CO_2 + 4H_2O$$

Decomposition reaction:

$$La_2O_3 + Co_3O_4 + BaO \rightarrow LaBaCoO_3 + CoO$$

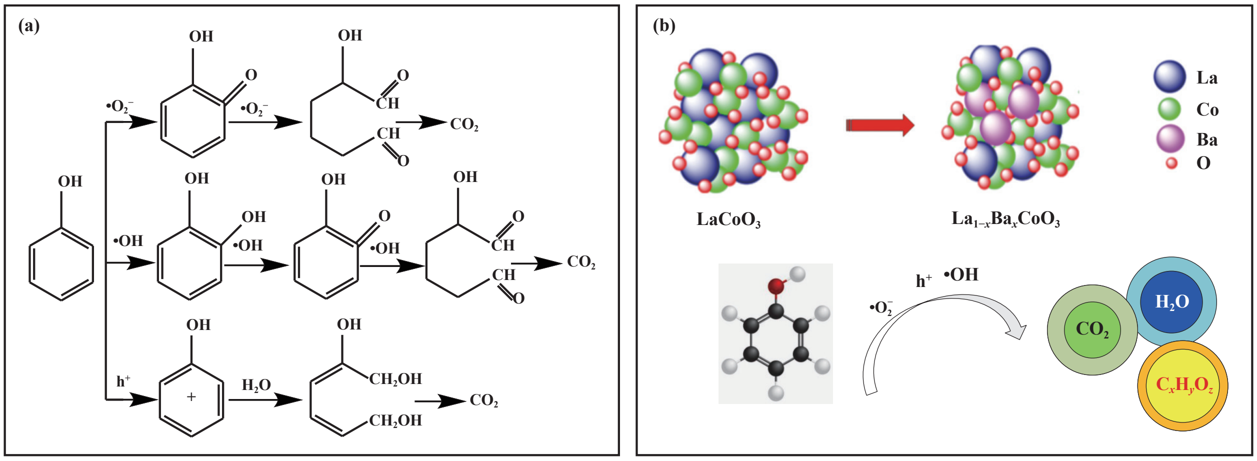

Fig.13 Three pathways of photocatalytic phenol degradation (a), and $La_{1-x}Ba_xCoO_3$ mechanism diagram (b)

3 Conclusions

A-site Ba-doped $La_{1-x}Ba_xCoO_3$ materials were successfully synthesized using a citric acid complexation-hydrothermal synthesis combined method. The physicochemical structures and properties of the resulting samples were characterized using XRD, SEM, BET and XPS. Among the synthesized materials, $La_{0.5}Ba_{0.5}CoO_3$ exhibited the highest phenol degradation rate (83.5%), following pseudo-first-order kinetics.

Various characterization techniques confirmed the successful incorporation of Ba into the $LaCoO_3$ crystal structure. While the morphology remained largely unchanged, a slight degree of agglomeration was observed in the modified catalyst. The specific surface area of the catalysts was relatively small and decreased with increasing Ba doping. Magnetization, as assessed by M-H curves, appeared to correlate with catalytic activity, with stronger magnetic intensity associated with better phenol photodegradation. The strong paramagnetism of the catalyst suggested good recyclability and potential cost savings. Notably, the Ba-0.5 catalyst retained high photocatalytic activity after five cycles, with XRD analysis confirming minimal structural changes. The XPS characterization results showed that Ba-0.5 had the highest oxygen content, and its oxygen vacancies made it positively charged, leading to an extension of the positron lifetime, reducing the recombination of electron-hole pairs, and enhancing the photocatalytic activity. Additionally, the magnetic properties of the photocatalyst were also related to its photocatalytic activity. A photocatalyst with certain magnetic properties could better adsorb the light source required for photocatalytic reactions, thereby improving photocatalytic activity. Furthermore, magnetism could also help in the recovery and reuse of the photocatalyst, reducing catalyst loss, and ultimately improving the economic and environmental friendliness of photocatalysis. The MPMS characterization results showed that Ba-0.5 has high magnetism, which helped to enhance its catalytic activity. In conclusion, Ba-0.5 had the highest photocatalytic activity.

The photocatalytic mechanism study suggested that electron-hole pairs convert surface-adsorbed oxygen into highly active free radicals (•OH and $•O_2^-$). Photogenerated holes migrate to the catalyst surface, where they participated in redox reactions with adsorbed phenol. The degradation of phenol was primarily driven by •OH radicals, with $•O_2^-$ and h^+ playing a supporting role. Under visible light irradiation, phenol was ultimately degraded into carbon dioxide, water, and small inorganic molecules through three distinct pathways.

References

[1] Eriksson E, Baun A, Mikkelsen, P S, *et al*. Risk assessment of xenobiotics in stormwater discharged to Harrestrup Å, Denmark[J]. *Desalination*, 2007, **215**(1/3): 187−197.

[2] Mahmoodi N M, Arami M, Limaee N Y, *et al*. Photocatalytic degradation of agricultural *N*-heterocyclic organic pollutants using immobilized nanoparticles of titania[J]. *J Hazard Mater*, 2007, **145**(1/2): 65−71.

[3] Esplugas S, Giménez J, Contreras S, *et al*. Comparison of different advanced oxidation processes for phenol degradation[J]. *Water Res*, 2002, **36**(4): 1034−1042.

[4] Matos J, Laine J, Herrmann J M. Synergy effect in the photocatalytic degradation of phenol on a suspended mixture of titania and activated carbon[J]. *Appl Catal B-Environ*, 1998, **18**(3/4): 281−291.

[5] Jeong W H, Lee H E, Ryu M W, *et al*. Phenol degradation on the surface of mesoporous TiO_2 particles via ligand-to-metal charge transfer under visible light irradiation[J]. *Chem Phys Lett*, 2024, **840**: 141162.

[6] Yang Q Z, Li X Q, Zhang S B, *et al*. ZnO hierarchical structures with tunable oxygen vacancies for high performance in photocatalytic degradation of phenol[J]. *J Mol Struct*, 2024, **1304**: 137656.

[7] Chu Y, Li X H, Ma J, *et al*. Nano polyoxometalate-based copper complex with double catalytic sites as heterogeneous catalyst for high-efficient degradation of phenol[J]. *Inorg Chem Commun*, 2024, **161**: 112123.

[8] Baruah M, Kumar S, Ezung S L, *et al*. Preparation of Co-doped TiO_2 activated carbon nanocomposite and its photocatalytic degradation of phenol wastewater[J]. *Inorg Chem Commun*, 2024, **166**: 112644.

[9] Jia X Y, Zhang J H, Huang Q L, *et al*. Heterogeneous catalytic degradation of phenol by $CuFe_2O_4/Bi_{12}O_{15}C_{16}$ photocatalyst activated peroxymonosulfate[J]. *Mater Res Bull*, 2023, **167**: 112435.

[10] Wei Y, Lei X F, Luo S H, *et al*. Effect of pore-forming agent on degradation of phenol by iron tailings based porous ceramics[J]. *Ceram Int*, 2024, **50**(18): 33791−33801.

[11] Wang Q, Li N Y, Tan M, *et al*. Novel dual Z-scheme $Bi/BiOI-Bi_2O_3-C_3N_4$ heterojunctions with synergistic boosted photocatalytic degradation of phenol[J]. *Sep Purif Technol*, 2023, **307**: 122733.

[12] Wang X P, Yang Z H, Jiang Y Q, *et al*. Adsorption and catalytic degradation of phenol in water by a Mn, N co-doped biochar via a non-radical oxidation process[J]. *Sep Purif Technol*, 2024, **330**: 125267.

[13] Fergus J W. Perovskite oxides for semiconductor-based gas sensors[J]. *Sens Actuator B-Chem*, 2007, **123**(2): 1169−1179.

[14] Sradhasagar S, Khuntia O S, Biswal S, *et al*. Machine learning-aided

discovery of bismuth-based transition metal oxide double perovskites for solar cell applications[J]. *Sol Energy*, 2024, **267**: 112209.

[15] Ali N, Ali M, Nawaz A, *et al*. Fabrication, characterization, metal ions sensor and photocatalytic activity of visible light harvesting lead free perovskite oxide[J]. *Mater Chem Phys*, 2024, **325**: 129738.

[16] Li W H, Sunarso J, Yang Y, *et al*. Strategies for improving oxygen ionic conducting in perovskite oxides and their practical applications[J]. *Energy Rev*, 2024, **3**(4): 100085.

[17] Schmidt L J. Contributed papers in specimen mineralogy: 38th Rochester mineralogical symposium abstracts: Part 3[J]. *Rocks Miner*, 2012, **87**(5): 444−454.

[18] Wang Y G, Xu G, Yang L L, *et al*. Enhanced ferromagnetic properties of multiferroic $BiCo_xFe_{1-x}O_3$ synthesized by hydrothermal method[J]. *Mater Lett*, 2008, **62**(23): 3806−3808.

[19] Fan Y, Wan C L, Zhao X M, *et al*. Ce-doped $LaMnO_{3-\delta}$ perovskite as an efficient ozonation catalyst for the degradation of high-concentration phenol wastewater[J]. *J Environ Chem Eng*, 2024, **12**(3): 112761.

[20] Huang L K, Di X Y, Wang G Z, *et al*. Fe element B-site doped lanthanum-copper perovskite type material for cellulosic ethanol wastewater treatment[J]. *Mater Chem Phys*, 2024, **313**: 128751.

[21] Bouchal W, Djani F, Mazouzi D E, *et al*. Bi-doped $BaBiO_3$ ($x = 0\%$, 5%, 10%, 15%, and 20%) perovskite oxides by a sol–gel method: Comprehensive biological assessment and RhB photodegradation[J]. *RSC Adv*, 2014, **14**(11): 7359−7370.

[22] Zhang H G, Shi H H, You H H, *et al*. Cu-doped $CaFeO_3$ perovskite oxide as oxygen reduction catalyst in air cathode microbial fuel cells[J]. *Eviron Res*, 2022, **214**: 113968.

[23] Vlazan P, Poienar, M, Malaescu I, *et al*. Exploiting the Bi-doping effect on the properties of $NaNbO_3$ perovskite-type materials[J]. *Chem Phys*, 2024, **579**: 112203.

[24] Li E B, Ma W, Zhang P, *et al*. The effect of Al^{3+} doping on the infrared radiation and thermophysical properties of $SrZrO_3$ perovskites as potential low thermal infrared material[J]. *Acta Mater*, 2021, **209**: 116795.

[25] Yang L P, Synthesis and photocatalytic properties of perovskite type composite oxides [D]. Taiyuan: Shanxi University, 2010.

[26] Hao C X, Wen F S, Xiang J Y, *et al*. Photocatalytic performances of $BiFeO_3$ particles with the average size in nanometer, submicrometer, and micrometer[J]. *Mater Res Bull*, 2014, **50**: 369−373.

[27] Tang C W, Wang C B, Chien S H. Characterization of cobalt oxides studied by FT-IR, Raman, TPR and TG-MS[J]. *Thermochim Acta*, 2008, **473**(1/2): 68−73.

[28] Abdel-Aal S K, Ouasri A. Crystal structures, hhirshfeld surfaces analysis, Infrared and Raman studies of organic-inorganic hybrid perovskite salts $NH_3(CH_2)_nNH_3MnCl_4$ (n=5, 6)[J]. *J Solid State Chem*, 2022, **314**: 123401.

[29] Bera J, Rout S K. On the formation mechanism of $BaTiO_3$-$BaZrO_3$ solid solution through solid-oxide reaction[J]. *Mater Lett*, 2005, **59**(1): 135−138.

[30] Li H H, Yu J Y, Gong Y S, *et al*. Perovskite catalysts with different dimensionalities for environmental and energy applications: A review[J]. *Sep Purif Technol*, 2023, **307**: 122716.

[31] Hong T M. Preparation and photocatalytic activity of iodine-doped TiO_2 and magnetic iodine-doped TiO_2 photocatalysts[D]. Hangzhou: Zhejiang University of Technology, 2012.

[32] Wang W A, Shi Q A, Wang Y P, *et al*. Preparation and characterization of iodine-doped mesoporous TiO_2 by hydrothermal method[J]. *Appl Surf Sci*, 2011, **257**(8): 3688−3696.

[33] Jiang H Q, Wang P, Lu D D, *et al*. Crystallite size, surface properties and photocatalytic activity of Gd^{3+}-doped TiO_2 nano-powder[J]. *J Chem Ind Eng (China)*, 2006, **57**(9): 2194−2200.

[34] Kucharczyk B, Tylus W. Effect of Pd or Ag additive on the activity and stability of monolithic $LaCoO_3$ perovskites for catalytic combustion of methane[J]. *Catal Today*, 2004, **90**(1/2): 121−126.

[35] Dudric R, Vladescu A, Rednic V, *et al*. XPS study on $La_{0.67}Ca_{0.33}Mn_{1-x}Co_xO_3$ compounds[J]. *J Mol Struct*, 2014, **1073**: 66−70.

[36] Stöcker M. X-Ray photoelectron spectroscopy on zeolites and related materials[J]. *Microporous Mat*, 1996, **6**(5/6): 235−257.

[37] Rangappa D, Fujiwara T, Watanabe T, *et al*. Preparation of $Ba_{1-x}Sr_xWO_4$ and $Ba_{1-x}Ca_xWO_4$ films on tungsten plate by mechanically assisted solution reaction at room temperature[J]. *Mater Chem Phys*, 2008, **109**(2/3): 217−223.

[38] Mašek K, Václavů M, Bábor P, *et al*. Sn-CeO_2 thin films prepared by rf magnetron sputtering: XPS and SIMS study[J]. *Appl Surf Sci*, 2009, **255**(13/14): 6656−6660.

[39] Zhang T J, Wang J, Zhang B S, *et al*. Preparation and dielectric properties of compositionally graded (Ba, Sr)TiO_3 thin film by sol-gel technique[J]. *Trans Nonferrous Met Soc China*, 2006, **16**: S119−S122.

[40] Mohanty B, Nayak N C, Parida B N, *et al*. Multifunctional characterization of multiferroic 0.5($NdFeO_3$)-0.5 ($Ba_{0.5}Sr_{0.5}TiO_3$) for storage and photovoltaics applications[J]. *Inorg Chem Commun*, 2023, **151**: 110588.

[41] Chen J, Wang P F, Kang Y, *et al*. Co_3O_4/$LaCoO_3$ nanocomposites derived from MOFs as anodes for high-performance lithium-ion batteries[J]. *Inorg Chem Commun*, 2022, **104**: 109447.

[42] Jin Z H, Hu R S, Wang H Y, *et al*. One-step impregnation method to prepare direct Z-scheme $LaCoO_3$/g-C_3N_4 heterojunction photocatalysts for phenol degradation under visible light[J]. *Appl Surf Sci*, 2019, **491**: 432−442.

[43] Peng S Q, Gan C, Yang Y, *et al*. Low temperature and controllable formation of oxygen vacancy $SrTiO_{3-x}$ by loading Pt for enhanced photocatalytic hydrogen evolution[J]. *Energy Technol*, 2018, **6**(11): 2166−2171.

[44] Wang Y G, Xu G, Ji X P, *et al*. Room-temperature ferromagnetism of Co-doped $Na_{0.5}Bi_{0.5}TiO_3$: Diluted magnetic ferroelectrics[J]. *J Alloy Compd*, 2019, **475**(1/20): L25−L30.

[45] Khan M I, Ali S M, Sahar M S U, *et al*. Analysis of cubic perovskite oxide $AgNbO_3$ under stress conditions: Potential for photovoltaic and high-temperature applications - A DFT study[J]. *Mater Sci Semicond Process*, 2024, **182**: 108711.

[46] Wang Y G. Hydrothermal synthesis, characterization and properties of perovskite oxide nanostructures [D]. Hangzhou: Zhejiang University, 2009.

[47] Sun M Z, Gao P Y, Wang M, *et al*. The effect of calcination temperature on the photocatalytic performance of Bi_2MoO_6 for the degradation of phenol under visible light[J]. *Optik*, 2019, **199**: 163319.

[48] Wang F, Wang X Q, Cheng K, *et al*. Effect of MoS_2 loading on photocatalytic degradation efficiency of phenol by MoS_2/TiO_2 and its mechanism[J]. *J Fuel Chem Technol*, 2017, **45**(8): 1001−1008.

[49] Dong Z M, Zhou R D, Xiong L Y, *et al*. Preparation of $Ti_{0.7}W_{0.3}O_2$@$BiVO_4$ *p-n* heterogeneous interfacial photocatalyst and mechanism of photodegradation of phenol by visible light[J]. *Acta Sci Circumstantiae*, 2020, **40**(5): 1674−1691.

[50] Wang S, Li Q, Gu X W, *et al*. Preparation and photocatalytic properties of AgI-BiOCl composites[J]. *Appl Chem Ind*, 2021, **7**(50): 1751−1756.

[51] Kuspanov Z, Umirzakov A, Serik A, *et al*. Multifunctional strontium titanate perovskitebased composite photocatalysts for energy conversion and other applications[J]. *Int J Hydrogen Energ*, 2023, **48**(98): 38634−38654.

[52] Wang X X, Guo S L, Niu Z Y, *et al*. Preparation of $LaCoO_3$ perovskite catalyst and its photocatalytic degradation of acid fuchsin and basic fuchsin[J]. *J Mol Catal (China)*, 2024, **38**(1): 71−80.

[53] Zhang X, Yao D N, Zhang H Y, *et al*. Construction of TiO_2@C/g-C_3N_4 and its photocatalytic degradation performance of tetracycline[J]. *J Mol Catal (China)*, 2024, **38**(4): 342−351.

[54] Li J, Li Q S. Synthesis and properties of two-dimensional composite photocatalyst[J]. *J Mol Catal (China)*, 2024, **38**(2): 99−103.

[55] Chen S T, Wang H, Cui W Q. Iron-doped bismuth sulfide PhotoFenton degrades organic pollutants[J]. *J Mol Catal (China)*, 2024, **38**(1): 17−25.

[56] Peng J W, Jiang Z T, Jiang K B, *et al*. Preparation of Z-scheme g-C_3N_4/Bi/BiOBr heterojunction photocatalyst and its visible light degradation of formaldehyde gas[J]. *J Mol Catal (China)*, 2023, **37**(1): 53−62.

[57] Wang Y X, Liu Y J, Tao R, *et al*. Preparation and photocatalytic properties of K/Cl doped g-C_3N_4[J]. *J Mol Catal (China)*, 2022, **36**(6): 561−570.

[58] Li C, Chen X F, Yue X, *et al*. Preparation of perovskite $LaFe_xCu_{(1-x)}O_3$ heterogeneous Fenton catalyst and its degradation of methylene blue[J]. *J Mol Catal (China)*, 2021, **35**(6): 503−517.

[59] Zhang H Y, Guo J W, Gong J R, *et al*. Study on the electronic structure modulation and photocatalytic performance of bismuth oxychloride photocatalysts[J]. *J Mol Catal (China)*, 2022, **36**(5): 433−445.

A 位钡掺杂钙钛矿型 $LaCoO_3$ 光催化剂制备及其光催化降解苯酚性能

袁利静[1], 赵坤峰[2], 宋　金[3], 郭世龙[3], 郭佳乐[3], 王　艳[3], 孟现洁[4], 卫贤贤[5], 刘振民[3], 王潇潇[3*]

（1. 太原科技大学 能源与材料工程学院, 山西 太原 030024; 2. 交通运输部东海航海保障中心温州航标处, 浙江 温州 325000;
3. 太原科技大学 化学工程与技术学院, 山西 太原 030024; 4. 太原理工大学 化学工程与技术学院, 山西 太原 030024;
5. 太原科技大学 环境与资源学院, 山西 太原 030024）

摘要: 钙钛矿氧化物材料作为光催化降解水中有机污染物催化剂的应用是一个前景广阔且快速发展的领域. 本文采用柠檬酸配合-水热合成相结合的方法合成出一系列不同 Ba 掺杂比的 $La_{1-x}Ba_xCoO_3$(x=0.2, 0.3, 0.4, 0.5, 0.6) 钙钛矿型光催化剂, 并考察其在可见光下光催化降解苯酚的催化性能. 实验结果表明 $La_{0.5}Ba_{0.5}CoO_3$ 表现出最高的光催化性能.此外, 还讨论了 $La_{0.5}Ba_{0.5}CoO_3$ 的光催化机理. 通过 X 射线衍射 (XRD)、扫描电子显微镜 (SEM)、傅里叶变换红外光谱 (FT-IR)、X 射线电子能谱 (XPS)、磁性测量系统 (MPMS) 等多种表征技术对合成的催化剂进行全面表征, 结果表明, $La_{1-x}Ba_xCoO_3$ 的衍射峰强度随着 Ba 掺杂比的增加而增强, 其中 $La_{0.4}Ba_{0.6}CoO_3$ 的衍射峰最强.催化剂颗粒大小范围为 10~50 nm, 且随着 Ba 含量的增加, 比表面积逐渐降低.此外, $La_{0.5}Ba_{0.5}CoO_3$ 和 $La_{0.4}Ba_{0.6}CoO_3$ 的顺磁性特征非常相似. 实验结果表明, Ba 的掺杂可以显著增强 $La_{1-x}Ba_xCoO_3$ 钙钛矿的催化性能, 促进电子循环和羟基自由基 (•OH) 的生成, 从而有效降解苯酚.

关键词: 钙钛矿催化剂; $La_{1-x}Ba_xCoO_3$; 光催化; 苯酚降解; 机理